NANO LETTERS

2006
Vol. 6, No. 8
1706−1710

Orthogonal Self-Assembly of Carbon Nanotube Crossbar Architectures by Simultaneous Graphoepitaxy and Field-Directed Growth

Ariel Ismach and Ernesto Joselevich*

Department of Materials and Interfaces, Weizmann Institute of Science, Rehovot 76100, Israel

Received May 3, 2006; Revised Manuscript Received July 4, 2006

ABSTRACT

Crossbar arrays of single-wall carbon nanotubes are produced spontaneously in a single step of chemical vapor deposition by simultaneous graphoepitaxy along faceted nanosteps and field-directed growth, perpendicular to each other. The two alignment mechanisms take place selectively on miscut C-plane sapphire and patterned amorphous SiO_2 islands, respectively, without mutual interference, producing dense nanotube grids, with up to 12 junctions per square micrometer. This one-step method of orthogonal self-assembly may open up new possibilities for nanotube circuit integration.

Single-wall carbon nanotubes (SWNTs) have unique electronic and mechanical properties,[1] which make them attractive building blocks for nanoelectronics.[2,3] During the last few years, a wide range of SWNT-based devices were made successfully.[4−11] However, the organization of SWNTs into horizontal arrays on surfaces, which represents a crucial prerequisite for large-scale device integration, remains a significant challenge. Approaches to carbon nanotube organization can be divided into three major groups: (a) Post-growth aligned deposition from liquid dispersions at specific locations and directions on the surface, by means of chemical modifications on either or both surface and nanotubes[12] under external forces generated by flow,[13] magnetic,[14] or electric[15] fields, and surface acoustic waves.[16] Although these methods have the advantages of *chemie douce*, the dispersion of nanotubes in liquid is difficult, normally requiring sonication, which shortens the nanotubes to lengths of 1−5 μm. Moreover, the intrinsic electrical and mechanical properties of the SWNTs are often damaged by both sonication and chemical modification. (b) Aligned growth under external forces, such as electric field[17−19] and gas flow.[20] (c) Epitaxial approaches, namely, surface-guided growth along lattice directions (lattice-directed epitaxy),[21−24] atomic steps (ledge-directed epitaxy),[25,26] and nanofacets (graphoepitaxy)[27] on single-crystal surfaces.

Crossbar architectures are especially desired for nanoelectronics because they constitute the basis of most logic and memory elements in computing devices.[4,28−33] A carbon nanotube-based nonvolatile random access memory based on a crossbar architecture was proposed;[4] however, the lack of an effective procedure for the production of such nanotube grids inhibited its actual development beyond the single-device level. Even if crossbar architectures may not be perfect, they have been shown to be potentially defect tolerant,[34] thus being compatible with fabrication by self-assembly. SWNTs crossbar arrays were assembled by means of electric fields,[15] gas flow,[20] and electrospinning.[35] However, typical problems of those methods are low junction density and the requirement of at least two separate steps of aligned growth or deposition.

Orthogonal self-assembly is referred to as the spontaneous organization of molecules into higher structures by different mechanisms occurring selectively and simultaneously without mutual interference.[36] Orthogonality enables the formation of complex structures in a single step, thus representing a higher order of self-assembly than that possible by a single-mechanism process. In this paper, we expand the concept of orthogonal self-assembly to the spontaneous formation of SWNT crossbar architectures by two independent alignment mechanisms. High-density SWNT grids form spontaneously in a single step of chemical vapor deposition (CVD) by a combination of graphoepitaxy along faceted nanosteps[27] and electric field-directed growth.[17,19]

Recently, we have shown that SWNTs grow along the 0.2-nm-high atomic steps of miscut C-plane sapphire surfaces,[25] that is, vicinal α-Al_2O_3 (0001). We also demonstrated the

* Corresponding author. E-mail: ernesto.joselevich@weizmann.ac.il. Tel: +972-8-934-2350. Department of Materials and Interfaces, Weizmann Institute of Science, Rehovot, 76100, Israel.

10.1021/nl0610026 CCC: $33.50
Published on Web 07/22/2006

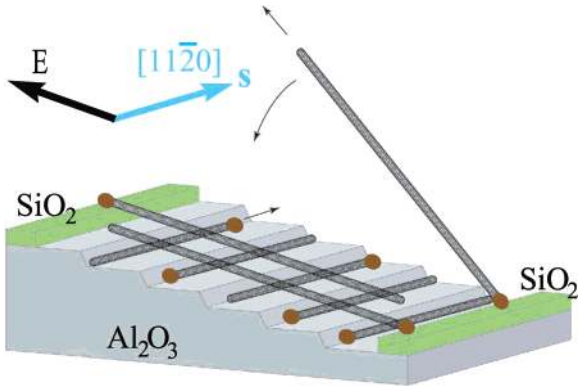

Figure 1. Schematic representation of the orthogonal self-assembly of a SWNT crossbar array by simultaneous graphoepitaxy and field-directed growth. The drawing shows the annealed miscut C-plane sapphire with nanosteps along the [11$\bar{2}$0] direction, while the electric field is applied perpendicularly to the steps. The nanotubes originating from catalyst nanoparticles (brown balls) lying on the sapphire (Al_2O_3) grow along the faceted nanosteps, while the nanotubes emerging from the catalyst on the patterned SiO_2 stripes grow freely without interacting with the surface, in a way that allows their alignment by the electric field, eventually falling across the nanotubes grown on the sapphire.

highly aligned growth of SWNTs along the 1.3−4-nm-high faceted nanosteps of annealed miscut C-pane sapphire.[27] The alignment of the SWNTs on these surfaces was shown to be unaffected by external forces, such as electric field and gas flow.[25,27] However, when the same substrates were precoated with a thin layer of amorphous SiO_2, the nanotubes were aligned by an applied electric field, as observed previously on Si/SiO_2 surfaces.[25] Following these observations, we concluded that the nanotubes growing on the miscut sapphire surfaces are aligned by a surface-growth mechanism, whereas the nanotubes growing on the amorphous SiO_2-coated surfaces grow up free without interacting with the surface, in a way that allows them to rotate and be aligned by the electric field before they settle down on the surface. To explain the aligned growth along the atomic steps and faceted nanosteps, we proposed a "wake-growth" mechanism,[25] in which each catalyst nanoparticle slides along the step, leaving the nanotube behind as a wake. The understanding that different alignment mechanisms can selectively take place on the same substrate with different treatments led us to the working hypothesis that we could exploit this selectivity to assemble SWNT complex architectures by a combination of these two mechanisms using patterned SiO_2 islands. A schematic representation of the orthogonal self-assembly of SWNT crossbar architectures is shown in Figure 1. The nanotubes originating from the catalyst nanoparticles lying on the bare sapphire grow along the nanosteps, while the nanotubes originating from catalyst nanoparticles lying on the amorphous SiO_2 islands grow up free and are aligned by the electric field, which is applied perpendicular to the steps.

The substrates for orthogonal growth are prepared by first cutting and polishing sapphire wafers with a miscut of ~4° from the C plane. Miscut toward [1$\bar{1}$00] at room temperature produces vicinal α-Al_2O_3 (0001) surfaces with atomic steps along [11$\bar{2}$0]. The substrates are later annealed for 10 h at

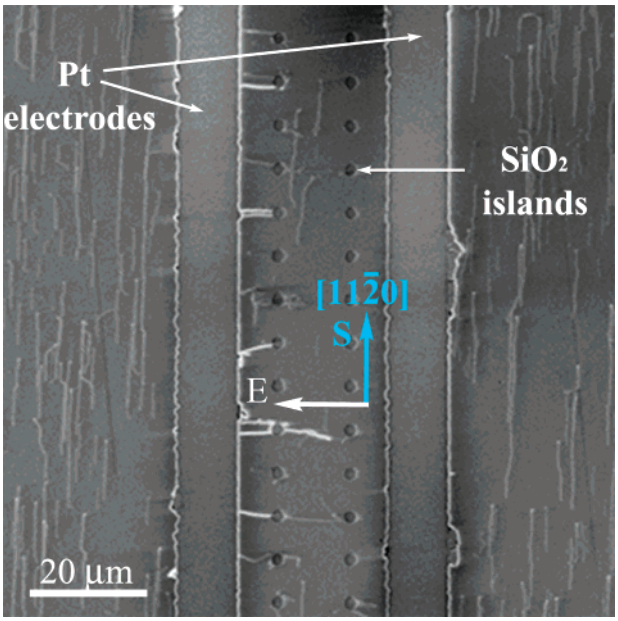

Figure 2. SEM image showing the aligned nanotubes along the nanosteps (step vector **s**), in the [11$\bar{2}$0] direction, whereas only the SWNTs emerging from the SiO_2 islands were aligned by the electric field (**E**, 2×10^6 V/m).

1100 °C in air. Upon annealing, the thermodynamically unstable atomic steps tend to reduce the surface energy by bunching together into faceted nanosteps spaced by flat C-plane terraces.[25,27] The height of the faceted nanosteps is determined by equilibrium between the elastic energy due to surface stress, and the energy of the facet edges,[38] reaching the 1.2−4 nm. For consistency throughout the experiments and figures, we have defined a step vector[25] $\mathbf{s} = \hat{\mathbf{c}} \times \hat{\mathbf{n}}$, where $\hat{\mathbf{c}}$ and $\hat{\mathbf{n}}$ are unit vectors normal to the C-plane (0001) and to the surface plane, respectively, so that **s** is parallel to the steps, descending to the right. The exact crystal orientation, as well as the miscut inclination and azimuth angles, were determined by both a previously reported technique of asymmetric double-exposure back-reflection X-ray diffraction (XRD)[25,27] and AFM topographic analysis, as shown in Figure S4 in the Supporting Information. After annealing, a first standard photolithography process was done to create the platinum electrodes that were used to apply the electric field during the SWNT growth. Then, a second photolithography was done to create stripes or square islands of 20-nm-thick amorphous SiO_2 (see the Supporting Information for experimental details). The nanotubes were grown by CVD, using ferritin as a catalyst, as described previously.[19,25]

Figure 2 shows a scanning electron microscopy (SEM) image where amorphous SiO_2 square islands were patterned between the Pt electrodes. Most of the nanotubes that have both ends on the bare sapphire surface are aligned along the nanosteps (not visible in the SEM image) in the [11$\bar{2}$0] direction, while a significant number of SWNTs lying parallel to the electric field between the electrodes have all or at least one end on a SiO_2 islands. This experiment demonstrates that the SiO_2 islands indeed lead to the formation of field-aligned nanotubes simultaneously with graphoepitaxial growth along the nanosteps, and the selectivity of the two different

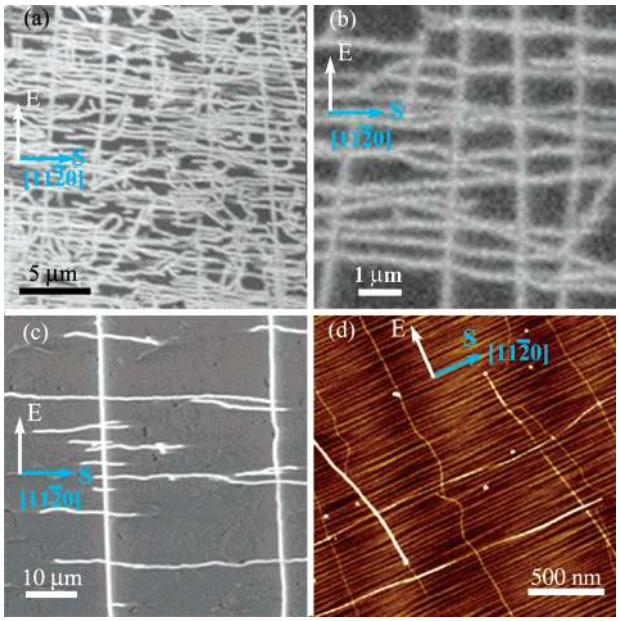

Figure 3. Dense SWNT grids obtained by simultaneous graphoepitaxy and field-directed growth. (a and b) SEM images at different magnifications of the same sample. (c) SWNT grid with a high density of graphoepitaxial nanotubes and a lower density of field-directed ones. (d) AFM topographic image showing the nanotube crossbar structure and the faceted nanosteps.

alignment mechanisms on the bare sapphire and the SiO_2-coated sapphire, respectively. However, the small size of the SiO_2 patterned islands yields a low density of field-directed grown SWNTs. High-density SWNT grids were obtained in a similar way, but by patterning continuous stripes of SiO_2, as shown in Figure 3. The nanotube density along the faceted steps is dictated mainly by the catalyst concentration and the nanoparticle and nanotube−step interaction, while their spacing depends on the miscut inclination and orientation angles, annealing time, and temperature. However, the density of the SWNTs along the electric field is dictated by the amount of free-grown nanotubes originating from the SiO_2 stripes. In principle, more sophisticated catalyst patterning methods could be used to grow nanotubes at specific locations and obtain denser and periodic SWNT grids.

A statistical analysis of the nanotube orientation in a dense orthogonally self-assembled crossbar array (sample shown in Figure 3a) is displayed in Figure 4. The angular distribution of the nanotubes (relative to the step vector **s**) between the electrodes is bimodal (Figure 4a), with two well-resolved peaks at 4 ± 8° and 100 ± 8°, which correspond to the directions of the nanosteps and the applied electric field, respectively. Far away from the electrodes (Figure 4b), where the influence of the electric field is very weak and no SiO_2 was deposited, the angular distribution shows a single peak at 1.2 ± 4°, indicating that all the nanotubes have grown along the nanosteps. Figure 4c shows the distribution of crossing angles between the nanotubes at the crossbar junctions, showing a normal distribution of 96 ± 12°. Cross densities of typically 7, and up to 12 per μm^2 were found on these samples.

Insight into the actual structure of the SWNT crossed junctions can be obtained from a detailed topographic

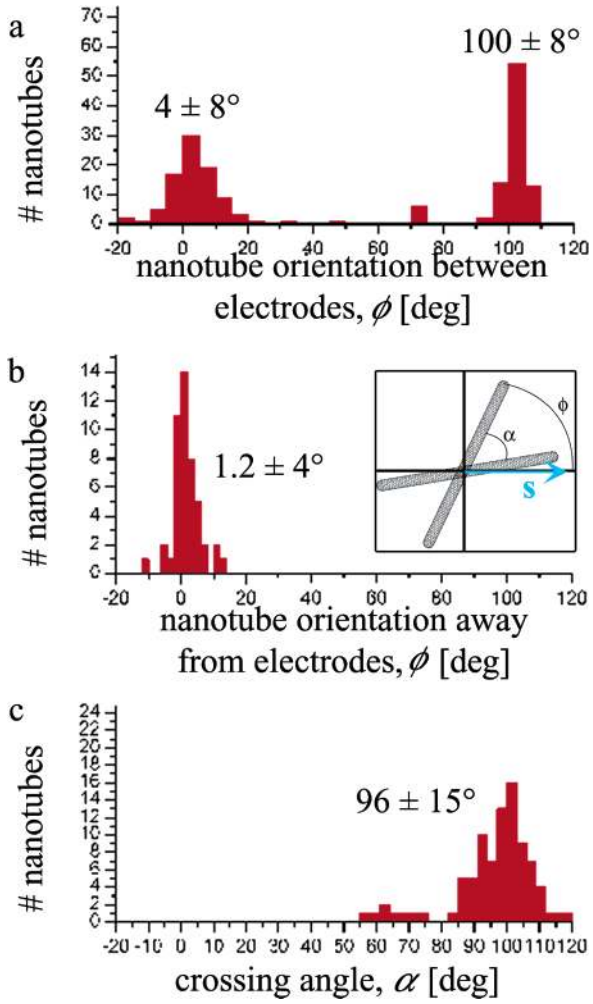

Figure 4. Histogram representing a statistical analysis of an orthogonally self-assembled SWNT crossbar array (sample shown in Figure 3a). (a) Nanotube angular distribution (relative to the step vector **s**) between the electrodes, where the electric field is high and the SiO_2 stripes were patterned. (b) Angular distribution far away from the electrodes, where the electric field is very weak and no SiO_2 was deposited. The inset shows the definition of the nanotube orientation ϕ and the crossing angle α. (c) Crossing angle distribution, showing a single peak at 96 ± 15°.

analysis by AFM, as shown in Figure 5. The graphoepitaxial nanotube chosen in this analysis is higher than the step, so it can be clearly seen. Otherwise, if the graphoepitaxial nanotubes are too thin, and thus lower than the nanosteps, they can hide by the step, and be seen only in certain parts where they occasionally stray off the nanofacet (see the Supporting Information). Figure 5a shows a 3D projection of the crossed junction between the graphoepitaxial nanotube and the field-directed nanotube. The latter is clearly on top of the former, as predicted by the orthogonal self-assembly mechanism (Figure 1). Interestingly, both nanotubes appear to be radially deformed at the junction. This is seen clearly in the section analyses of Figure 5b and c, where the red and green curves represent the topographic profiles at the junction along the field-directed and graphoepitaxial nanotubes, respectively. The black curves in each graph represent parallel section analyses about 100 nm away from the junction. From these section analyses, the height of the

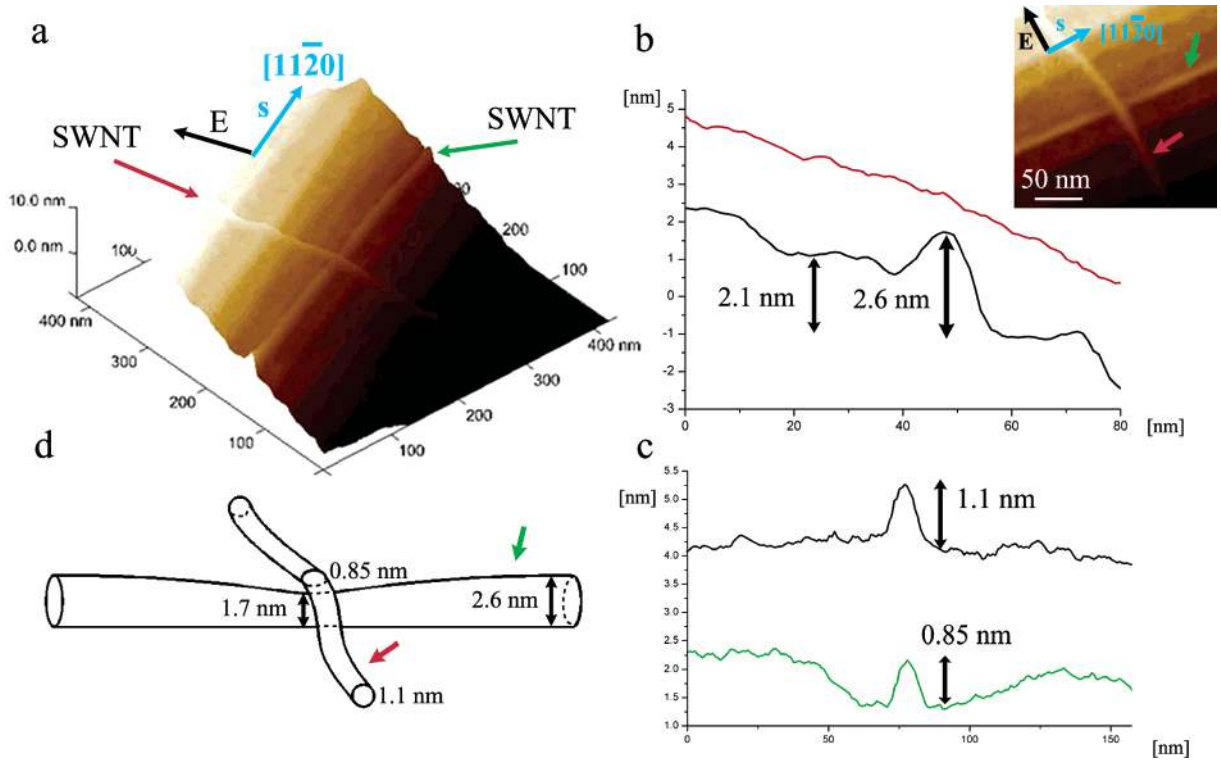

Figure 5. Topographic analysis of a nanotube crossbar junction by AFM. (a) 3D projection showing the graphoepitaxial nanotube along the step vector **s**, and the field-directed nanotube along the electric field vector **E**. (b) Topographic section along the field-directed nanotube at the junction (red curve) and ca. 100 nm away from the junction (black curve), showing the heights of the step (2.1 nm) and the graphoepitaxial nanotube (2.6 nm). (c) Topographic section along the graphoepitaxial nanotube at the junction (green curve) and ca. 100 nm away from the junction (black curve), showing the heights of the field-directed nanotube at the junction (0.85 nm) and away from the junction (1.1 nm). (d) Scale model of the nanotube crossbar junction based on the topographic analysis.

nanostep is 2.1 nm. The height of the graphoepitaxial nanotube and the field-directed nanotube away from the junction are 2.6 and 1.1 nm, respectively, but the height of the junction is 2.9 nm, which represents a compression of 22% with respect to the sum of the heights of the two nanotubes away from the junction (3.7 nm). As shown in Figure 5c, the height of the field-directed nanotube at the junction is 0.85 nm. Considering the junction height and assuming an intertube distance of 0.34 nm, the height of the graphoepitaxial nanotube at the junction is 1.7 nm. A scale model of the junction is represented in Figure 5d. The graphoepitaxial and the field-directed nanotubes are thus radially compressed at the junction with reductions of 35% and 23%, respectively, from their diameter. On the basis of reported theoretical calculations,[38,39] and considering the diameters of the nanotubes, these radial compressions are both consistent with an estimated force of 6 nN at the junction, were the thinner nanotube is more radially rigid than the thicker one. These types of deformations have been studied both theoretically[40] and experimentally[41,42] and have shown to locally modify the electronic properties of the nanotubes. Depending on the relation between the step height and the nanotube diameter, we can have either compressed junctions, such as the one shown in Figure 5, or gapped junctions, where the upper and lower nanotubes are physically separated by the step. In our samples, step heights vary from 1.3 to 4 nm, whereas nanotube diameters vary from 0.8 to 3 nm. It is difficult to perform an unbiased statistical analysis of the diameter distribution because of the interference of the steps, by which some of the nanotubes are often hidden, and the possibility that some of the thicker nanotubes may be double-walled must also not be completely ruled out. In any case, the electrical and possible electromechanical properties of these junctions are an interesting topic of future studies.

In summary, we have demonstrated that orthogonal self-assembly of SWNT crossbar architectures can be accomplished in a single CVD step by a combination of two independent alignment methods, namely, graphoepitaxy by faceted nanosteps and electric field-directed growth. In principle, any combination of external forces (electric field, gas flow) and nanotube epitaxy (lattice-directed, ledge-directed, graphoepitaxy) should allow orthogonal self-assembly of crossbar architectures. This single-step process leads to a high density of nanotube crosses, which may enable new fundamental research and future large-scale technological applications of carbon nanotubes in nanoelectronics.

Acknowledgment. This research was supported by the U.S.−Israel Binational Science Foundation, the Israel Science Foundation, the Kimmel Center for Nanoscale Science, and the Djanogly and Alhadeff foundations. E.J. holds the Victor Erlich Career Development Chair.

Supporting Information Available: Definitions of miscut parameters, the resulting morphologies of nanotube

graphoepitaxy, and methods. This material is available free of charge via the Internet at http://pubs.acs.org.

References

(1) Dresselhaus, M. S.; Dresselhaus, G.; Avouris, P. *Carbon Nanotubes: Synthesis, Properties, and Applications*; Springer: Heidelberg, 2004.
(2) *Nanoelectronics and Information Technology*; Rainer, W., Ed.; Wiley-VCH: Weinheim, Germany, 2003.
(3) Avouris, P. *Acc. Chem. Res.* **2002**, *35*, 1026−1034.
(4) Rueckes, T.; Kim, K.; Joselevich, E.; Tseng, G. Y.; Cheung, C. L.; Lieber, C. M. *Science* **2000**, *289*, 94−97.
(5) Bachtold, A.; Hadley, P.; Nakanishi, T.; Dekker, C. *Science* **2001**, *294*, 1317−1320.
(6) Sazonova, V.; Yaish, Y.; Ustunel, H.; Roundy, D.; Arias, T. A.; Mceuen, P. L. *Nature* **2004**, *431*, 284−287.
(7) Regan, B. C.; Aloni, S.; Ritchie, R. O.; Dahmen, U.; Zettl, A. *Nature* **2004**, *428*, 924−927.
(8) Fennimore, A. M.; Yuzvinsky, T. D.; Han, W. Q.; Fuhrer, M. S.; Cumings, J.; Zettl, A. *Nature* **2003**, *424*, 408−410.
(9) Yao, Z.; Postma, H. W. C.; Balents, L.; Dekker, C. *Nature* **1999**, *402*, 273−276.
(10) Snow, E. S.; Perkins, F. K.; Houser, E. J.; Badescu, S. C.; Reinecke, T. L. *Science* **2005**, *307*, 1942−1945.
(11) Postma, H. W. C.; Teepen, T.; Yao, Z.; Grifoni, M.; Dekker, C. *Science* **2001**, *293*, 76−79.
(12) Liu, J.; Casavant, M. J.; Cox, M.; Walters, D. A.; Boul, P.; Lu, W.; Rimberg, A. J.; Smith, K. A.; Colbert, D. T.; Smalley, R. E. *Chem. Phys. Lett.* **1999**, *303*, 125−129.
(13) Park, J. U.; Meitl, M. A.; Hur, S. H.; Usrey, M. L.; Strano, M. S.; Kenis, P. J. A.; Rogers, J. A. *Angew. Chem., Int. Ed.* **2006**, *45*, 581−585.
(14) Long, D. P.; Lazorcik, J. L.; Shashidhar, R. *Adv. Mater.* **2004**, *16*, 814.
(15) Diehl, M. R.; Yaliraki, S. N.; Beckman, R. A.; Barahona, M.; Heath, J. R. *Angew. Chem., Int. Ed.* **2001**, *41*, 353.
(16) Strobl, C. J.; Schaflein, C.; Beierlein, U.; Ebbecke, J.; Wixforth, A. *Appl. Phys. Lett.* **2004**, *85*, 1427−1429.
(17) Zhang, Y. G.; Chang, A. L.; Cao, J.; Wang, Q.; Kim, W.; Li, Y. M.; Morris, N.; Yenilmez, E.; Kong, J.; Dai, H. J. *Appl. Phys. Lett.* **2001**, *79*, 3155−3157.
(18) Radu, I.; Hanein, Y.; Cobden, D. H. *Nanotechnology* **2004**, *15*, 473−476.
(19) Joselevich, E.; Lieber, C. M. *Nano Lett.* **2002**, *2*, 1137−1141.
(20) Huang, S. M.; Maynor, B.; Cai, X. Y.; Liu, J. *Adv. Mater.* **2003**, *15*, 1651.
(21) Ago, H.; Nakamura, K.; Ikeda, K.; Uehara, N.; Ishigami, N.; Tsuji, M. *Chem. Phys. Lett.* **2005**, *408*, 433−438.
(22) Tominaga, M.; Ohira, A.; Kubo, A.; Taniguchi, I.; Kunitake, M. *Chem. Commun.* **2004**, 1518−1519.
(23) Su, M.; Li, Y.; Maynor, B.; Buldum, A.; Lu, J. P.; Liu, J. *J. Phys. Chem. B* **2000**, *104*, 6505−6508.
(24) Han, S.; Liu, X.; Zhou, C. *J. Am. Chem. Soc.* **2005**, *127*, 5294−5295.
(25) Ismach, A.; Segev, L.; Wachtel, E.; Joselevich, E. *Angew. Chem., Int. Ed.* **2004**, *43*, 6140−6143.
(26) Kocabas, C.; Hur, S. H.; Gaur, A.; Meitl, M. A.; Shim, M.; Rogers, J. A. *Small* **2005**, *1*, 1110−1116.
(27) Ismach, A.; Kantorovich, D.; Joselevich, E. *J. Am. Chem. Soc.* **2005**, *127*, 11554−11555.
(28) Fuhrer, M. S.; Nygard, J.; Shih, L.; Forero, M.; Yoon, Y. G.; Mazzoni, M. S. C.; Choi, H. J.; Ihm, J.; Louie, S. G.; Zettl, A.; Mceuen, P. L. *Science* **2000**, *288*, 494−497.
(29) Huang, Y.; Duan, X. F.; Cui, Y.; Lauhon, L. J.; Kim, K. H.; Lieber, C. M. *Science* **2001**, *294*, 1313−1317.
(30) Huang, Y.; Duan, X. F.; Wei, Q. Q.; Lieber, C. M. *Science* **2001**, *291*, 630−633.
(31) Melosh, N. A.; Boukai, A.; Diana, F.; Gerardot, B.; Badolato, A.; Petroff, P. M.; Heath, J. R. *Science* **2003**, *300*, 112−115.
(32) Zhong, Z. H.; Wang, D. L.; Cui, Y.; Bockrath, M. W.; Lieber, C. M. *Science* **2003**, *302*, 1377−1379.
(33) Nojeh, A.; Lakatos, G. W.; Peng, S.; Cho, K.; Pease, R. F. W. *Nano Lett.* **2003**, *3*, 1187−1190.
(34) Heath, J. R.; Kuekes, P. J.; Snider, G. S.; Williams, R. S. *Science* **1998**, *280*, 1716−1721.
(35) Gao, J. B.; Yu, A. P.; Itkis, M. E.; Bekyarova, E.; Zhao, B.; Niyogi, S.; Haddon, R. C. *J. Am. Chem. Soc.* **2004**, *126*, 16698−16699.
(36) Laibinis, P. E.; Hickman, J. J.; Wrighton, M. S.; Whitesides, G. M. *Science* **1989**, *245*, 845−847.
(37) Schukin, V.; Ledenstov, N.; Bimberg, D. *Epitaxy of Nanostructures*; Springer: Berlin, 2005.
(38) Hertel, T.; Walkup, R.; Avouris, P. *Phys. Rev. B* **1998**, *58*, 13870−13873.
(39) Lordi, V.; Yao, N. *J. Chem. Phys.* **1998**, *109*, 2509−2512.
(40) Gülseren, O.; Yildirim, T.; Ciraci, S.; Kılıç, Ç. *Phys. Rev. B* **2002**, *65*, 155410.
(41) Gómez-Navarro, C.; de Pablo, P. J.; Gómez-Herrero, J. *Adv. Mater.* **2004**, *16*, 549−552.
(42) Vitali, L.; Burghard, M.; Wahl, P.; Schneider, M. A.; Kern, K. *Phys. Rev. Lett.* **2006**, *96*, 086804.

NL0610026

Orthogonal Self-Assembly of Carbon Nanotube Crossbar Architectures by Simultaneous Graphoepitaxy and Field-Directed Growth

Ariel Ismach and Ernesto Joselevich*

Department of Materials and Interfaces, Weizmann Institute of Science, Rehovot 76100, Israel.

E-mail: ernesto.joselevich@weizmann.ac.il

Supporting Information

1. Definition of the miscut parameters

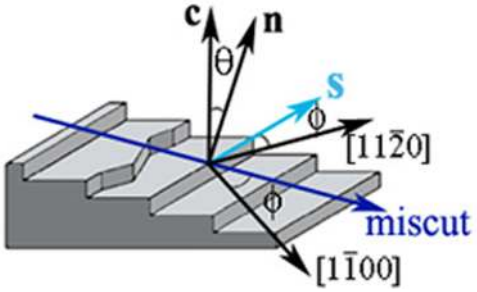

Figure S1. Miscut inclination and azimuth angles, θ and ϕ, respectively, and step vector **s**. The step vector is defined as $\mathbf{s} = \hat{\mathbf{c}} \times \hat{\mathbf{n}}$, where $\hat{\mathbf{c}}$ and $\hat{\mathbf{n}}$ are unit vectors normal to the C-plane and to the surface plane, respectively, so that **s** is parallel to the steps, descending to the right, and its modulus is the slope of the steps.

2. Sapphire faceting

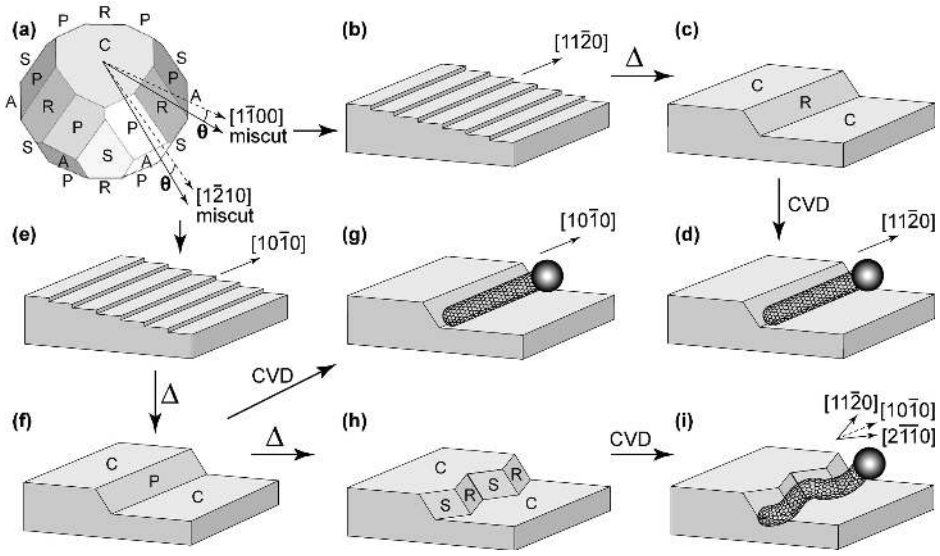

Figure S2. Possible morphologies of carbon nanotube graphoepitaxy obtained by miscut of C-plane sapphire, annealing, and CVD. (a) Equilibrium shape of α-Al_2O_3, with facets C$\{0001\}$, R$\{1\bar{1}02\}$, S$\{10\bar{1}1\}$, P$\{11\bar{2}3\}$, and A$\{11\bar{2}0\}$, in order of increasing surface energy. The same drawing is used to show the different miscut directions. (b) Miscut toward $[1\bar{1}00]$ produces a vicinal α-Al_2O_3 (0001) surface with atomic steps along $[11\bar{2}0]$. (c) Annealing leads to R-faceted nanosteps. (d) SWNTs grow straight along $[11\bar{2}0]$ (the ball represents the catalyst nanoparticle). (e) Miscut toward $[1\bar{2}10]$ produces a vicinal α-Al_2O_3 (0001) with atomic steps along$[10\bar{1}0]$. (f) Annealing initially leads to metastable P-faceted nanosteps. (g) SWNTs grow straight along$[10\bar{1}0]$. (h) Further annealing from (f) leads to sawtooth-shaped S/R-faceted nanosteps. (i) SWNTs grow loosely conformal to the sawtooth nanosteps, with segments along $[11\bar{2}0]$ and $[2\bar{1}\bar{1}0]$.

3. Methods

C-plane sapphire wafers were purchased from Gavish Industrial & Materials LTD., Omer, Israel (one side polished), with a miscut inclination angles of 4º towards the $[1\bar{1}00]$ direction. The material was received first as an ingot. The lattice orientation was identified by a back-reflection x-ray diffraction (XRD) method (see Figure S3 showing a XRD pattern from a α-Al_2O_3 (0001) sample). After marking the exact directions, the ingots were sent back to Gavish Company for cutting according to the specifications described above, and mechanical polishing. The miscut inclination and azimuth angles were determined by X-ray diffraction, by an asymmetric double-exposure back-reflection method[25] (see Figure S4a). The X-rays were produced by an Elliot GX6 rotating anode generator operating at 1.2 KW and producing Cu radiation with a 200 μm focus, with smallest wavelength of 0.41Å through k_α (1.54 Å) and residual lower intensities of larger wavelengths. The sample, placed perpendicular to the X-ray beam, was first exposed to back reflections for 2 hrs, and then rotated by 180º for a second exposure of 1 hr. In most cases a back reflection Laue pattern would have a larger number of reflections, which would be difficult to interpret. In order to reduce the number of spots and thus facilitate the recognition of both

patterns, from the first and second exposures, a nickel filter was used to cut off the k_β 1.39Å and shorter radiations. We know that 80% of the reflections are from radiation wavelengths between 1.5-1.8 Å. The miscut angle θ was measured by a systematic and an approximated method, both giving the same results: (i) The spots of the XRD patterns were placed on an appropriate Greninger chart in order to read the angular relations on the back reflection film, and then the spots were plotted on a stereographic projection to measure the miscut inclination and azimuth; (ii) The distance between the centers of the first and second patterns was measured and defined as 2*R*. Then the miscut inclinations given by $\theta = \tan^{-1}(2R/L)/4$, where L =3 cm is the distance between the sample and the X-ray sensitive film (7x7 cm) on which the Laue patterns were recorded. The result from such characterization is shown in Figure S4a. The green and red pattern represents the first, long, and second, short, exposures respectively. The miscut and azimuth angles where found to be $\theta = 4.3 \pm 0.4°$ and $\phi = 2 \pm 5°$ respectively. In addition, an independent AFM based method[25] was utilized to characterize the miscut of the samples used in the present study. Figure S4b shows the AFM characterization of an annealed sample. The graph is a section analysis across the steps (red line in the inset), showing the step height, *H*, and the distance between the steps, *D*. Then the miscut can be calculated[25] from the following relation $\theta = \sin^{-1}(H/D)$. By doing a statistical analysis of the heights of 50 steps, the miscut angle was found to be $\theta = 3.9 \pm 0.5°$.

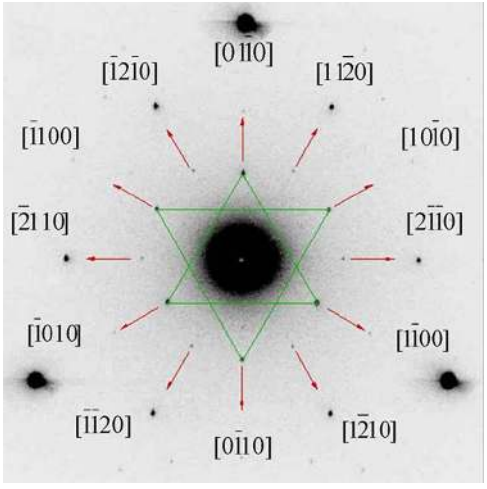

Figure S3. Back reflaction XRD pattern of a low-miscut α-Al_2O_3 (0001) surface, showing the different low-index lattice directions.

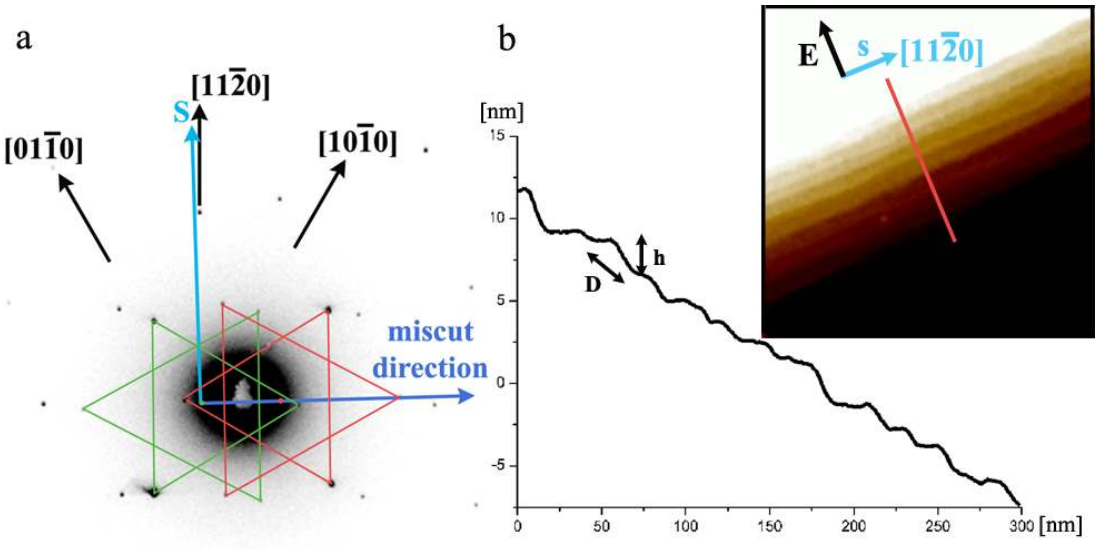

Figure S4. Characterization of the vicinal α-Al_2O_3 (0001) surface. (a) Double-exposure back-reflection XRD analysis showing the relevant lattice directions, step vector (**s**), and the miscut direction. The green and red patterns represent the first (long) and second (short) exposures respectively. It can be seen that the step vector is slightly deviated from the $[11\bar{2}0]$ direction, with a miscut azimuth angle of ϕ = 2 ± 5°. The miscut inclination angle is found to be θ = 4.3 ± 04°. (b) AFM characterization of the same surface after annealing (1100° C for 10 hrs). The staircase line represents a section analysis across the steps (red line in the inset AFM image). The spacing between the steps, D, and their height, H, are also shown for one step. By doing a statistical analysis on about 50 steps, the computed miscut angle is $\theta = \sin^{-1}(H/D) = 3.9 \pm 0.5°$.

The first photolithographic step was carried out to deposit the Pt electrodes (photoresist Microposit S1805, Shipley), followed by electron beam evaporation (Edwards Auto 306) of 10 nm titanium (99.99%, Holland Moran Ltd., Israel) and 90nm platinum (99.99%, Holland Moran Ltd. Israel), while cooled with liquid nitrogen. The second photolithographic step was done in order to pattern the amorphous SiO_2 islands or stripes. Then a thin layer, 10-20 nm, of SiO_2 (99.99%, Kurt J. Lesker) was deposited by electron beam evaporation (Edwards Auto 306). The lithographic electrodes were

connected with 4523AD Kulicke & Soffa wire bonder, to external electrodes. A DC voltage of 50 V was applied between the electrodes (separation 25 μm) during CVD.

Single-wall carbon nanotubes (SWNTs) were grown by catalytic chemical vapor deposition (CVD), using ferritin protein as a precursor for monodisperse Fe nanoparticle catalyst, as previously reported[19,25,27]. Substrates were first oxidized by oxygen plasma (March Plasmod GCM 200, 1-3 min, with 1 sccm of O_2), a ferritin solution of 0.1g/L (horse spleen ferritin, Sigma) was deposited on the samples for 10 min, washed with deionizied water and blow dried, followed by a second plasma oxidation step, to eliminate all the organic matter. Finally, the CVD was carried out at 800ºC for 10 min with a mixture of 60% Ar (99.998%, Oxygen & Argon Industries, Israel), 40% H_2 (99.999%, Gordon Gas, Israel) and 0.2% ethylene (99.9%, Gordon Gas, Israel) at 1 atm and flow rate of 1 L/min.

Atomic force microscopy (AFM) characterization was carried out in air tapping mode (Veeco, Multimode Nanoscope IV), using 70 kHz etched Si probes (FESP, Nanoprobes).

Scanning Electron Microscopy (SEM), Supra 55VP FEG LEO, characterization was done in low working voltages, 0.5-5kV.

4. Additional images of SWNT crossbar arrays from different samples

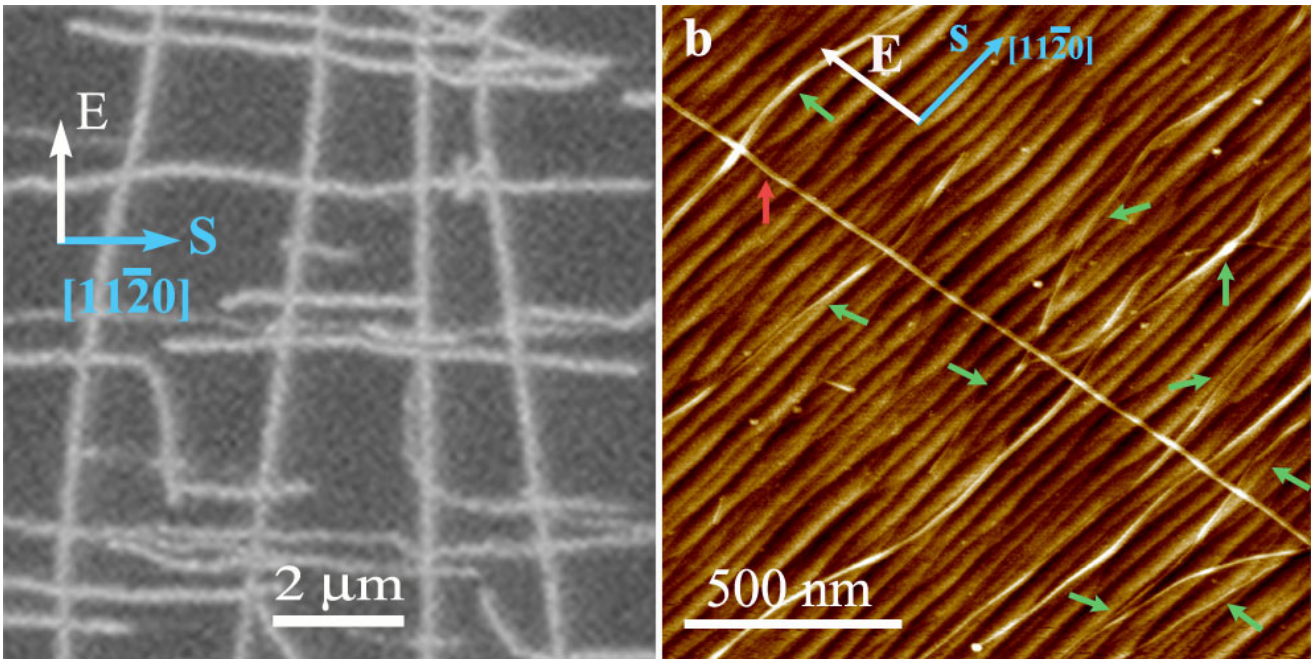

Figure S5. (a) SEM image showing a SWNTs grid structure produced by the orthogonal self-assembly process. (b) AFM topographic image in which a single nanotube aligned by the electric field (red arrow), crosses 9 graphoepitaxially aligned SWNTs (green arrows). Parts of the nanotubes can be seen hiding along the steps, which means that perhaps some nanotubes might be completely hidden by the stepped topography.